



HAL
open science

Can we detect the effect of spines and leaflets on the diffusion of brain intracellular metabolites?

Marco Palombo, Clémence Ligneul, Edwin Hernandez-Garzon, Julien Valette

► To cite this version:

Marco Palombo, Clémence Ligneul, Edwin Hernandez-Garzon, Julien Valette. Can we detect the effect of spines and leaflets on the diffusion of brain intracellular metabolites?. *NeuroImage*, 2018, 182, pp.283-293. 10.1016/j.neuroimage.2017.05.003 . cea-02155338

HAL Id: cea-02155338

<https://cea.hal.science/cea-02155338>

Submitted on 13 Jun 2019

HAL is a multi-disciplinary open access archive for the deposit and dissemination of scientific research documents, whether they are published or not. The documents may come from teaching and research institutions in France or abroad, or from public or private research centers.

L'archive ouverte pluridisciplinaire **HAL**, est destinée au dépôt et à la diffusion de documents scientifiques de niveau recherche, publiés ou non, émanant des établissements d'enseignement et de recherche français ou étrangers, des laboratoires publics ou privés.



Contents lists available at ScienceDirect

NeuroImage

journal homepage: www.elsevier.com/locate/neuroimage

Can we detect the effect of spines and leaflets on the diffusion of brain intracellular metabolites?

Marco Palombo^{a,b,c,*}, Clemence Ligneul^{a,b}, Edwin Hernandez-Garzon^{a,b}, Julien Valette^{a,b}

^a Commissariat à l'Energie Atomique et aux Energies Alternatives (CEA), Direction de la Recherche Fondamentale (DRF), Institut de Biologie François Jacob, MIRCen, F-92260 Fontenay-aux-Roses France

^b Centre National de la Recherche Scientifique (CNRS), Université Paris-Sud, Université Paris-Saclay, UMR 9199, Neurodegenerative Diseases Laboratory, F-92260 Fontenay-aux-Roses, France

^c Department of Computer Science and Centre for Medical Image Computing, University College of London, Gower Street, London WC1E 6BT, United Kingdom

ARTICLE INFO

Keywords:

Brain microstructure
Diffusion-weighted NMR
Diffusion-weighted NMR imaging
Diffusion-weighted NMR spectroscopy
Metabolite diffusion
Cell morphology

ABSTRACT

Prior models used to clarify which aspects of tissue microstructure mostly affect intracellular diffusion and corresponding diffusion-weighted magnetic resonance (DW-MR) signal have focused on relatively simple geometrical descriptions of the cellular microenvironment (spheres, randomly oriented cylinders, etc...), neglecting finer morphological details which may have an important role. Some types of neurons present high density of spines; and astrocytes and macroglial cells processes present leaflets, which may all impact the diffusion process. Here, we use Monte-Carlo simulations of many particles diffusing in cylindrical compartments with secondary structures mimicking spines and leaflets of neuronal and glial cell fibers, to investigate to what extent the diffusion-weighted signal of intracellular molecules is sensitive to spines/leaflets density and length. In order to study the specificity of DW-MR signal to these kinds of secondary structures, beading-like geometry is simulated as "control" deviation from smooth cylinder too. Results suggest that: a) the estimated intracellular tortuosity increases as spines/leaflets density or length (beading amplitude) increase; b) the tortuosity limit is reached for diffusion time $t_d > 200$ ms for metabolites and $t_d > 70$ ms for water molecules, suggesting that the effects of these finer morphological details are negligible at t_d longer than these threshold values; c) fiber diameter is overestimated, while intracellular diffusivity is underestimated, when simple geometrical models based on hollow smooth cylinders are used; d) apparent surface-to-volume, S/V, ratio estimated by linear fit of high frequency OG data appears to be an excellent estimation of the actual S/V ratio, even in the presence of secondary structures, and it increases as spines and leaflets density or length increase (while decreasing as beadings amplitude increases). Comparison between numerical simulations and multimodal metabolites DW-MRS experiments *in vivo* in mouse brain shows that these fine structures may affect the DW-MRS signal and the derived diffusion metrics consistently with their expected density and geometrical features.

This work suggests that finer structures of cell morphology have non-negligible effects on intracellular molecules' diffusion that may be measured by using multimodal DW-MRS approaches, stimulating future developments and applications.

Introduction

Diffusion-weighted MR imaging (DW-MRI) and spectroscopy (DW-MRS) are noninvasive techniques that provide the unique ability to characterize the microstructure of living as well as excised tissue (Basser et al., 1994; Beaulieu, 2002; Basser and Pierpaoli, 2011; Wedeen et al., 2012; Norris, 2001). DW-MRS, in particular, allows

quantifying the translational displacement of endogenous metabolites *in vivo* (Nicolay et al., 2001; Ronen and Valette, 2015). In contrast to water molecules, which are ubiquitous in biological tissues, most brain metabolites are confined into specific intracellular space: N-acetyl-aspartate (NAA) and glutamate (Glu) reside essentially in neurons, whereas myo-inositol (Ins) and choline (tCho) are thought to be glial markers preferentially compartmentalized in astrocytes (Choi et al.,

* Corresponding author at: Department of Computer Science and Centre for Medical Image Computing, University College of London, Gower Street, London WC1E 6BT, United Kingdom.

E-mail address: mrc.palombo@gmail.com (M. Palombo).

<http://dx.doi.org/10.1016/j.neuroimage.2017.05.003>

Accepted 3 May 2017

1053-8119/ © 2017 Elsevier Inc. All rights reserved.

2007). Under normal conditions, brain metabolites hardly cross the biological membranes so that their diffusion path is mainly dictated by intracellular features such as cytosol viscosity, molecular crowding, cell size and shape.

It has been recently shown that the apparent diffusion coefficient (ADC) of these intracellular metabolites in the primate brain and human gray (GM) and white matter (WM) is quite constant as the diffusion time t_d is increased from a few tens of ms to ~ 1 s (Najac et al., 2014, 2016). This suggests that the vastest fraction of each metabolite pool is not restricted in small subcellular domains (cell bodies, organelles...) but is instead diffusing along cell fibers. Performing metabolites ADC measurements for the same metabolites at ultra-long t_d (~ 2 s) *in vivo* in mouse and macaque brains and modeling brain cells as long and thin fibers with some finite length and number of successive embranchments, we recently extracted brain cell morphology in agreement with histological data, thus consolidating the metabolites cell-specific compartmentalization and the view that metabolites are diffusing in fibers (Palombo et al., 2016a). Above measurements of ADC as a function of t_d were all performed at relatively low b value (~ 3 ms/ μm^2 , i.e. weak gradient strength), where diffusion attenuation can be considered as monoexponential. However, it has been showed that, for the same metabolites, diffusion at very high b (i.e. strong gradient strength) exhibits a non-monoexponential behavior in the brain (Ligneul et al., 2016; Palombo et al., 2016b; Assaf and Cohen, 1999, 2000; Pfeuffer et al., 2000; Cohen and Assaf, 2002; Bar-Shir and Cohen, 2008; Kroenke et al., 2004; Yablonskiy and Sukstanskii, 2010a). We recently investigated how diffusion of these metabolites measured *in vivo* in the healthy mouse brain up to very high q ($1 \mu\text{m}^{-1}$) at relatively short t_d (63.2 ms), corresponding to very high b=60 ms/ μm^2 , can be explained by the (admittedly) simplistic view of diffusion in cylinders (Palombo et al., 2016b). We modeled cell fibers as isotropically oriented cylinders of infinite length and finite diameter, and showed this can account very well for measured non-monoexponential attenuation, yielding fiber radii and intracellular metabolites diffusivities in the expected ranges (0.5–1.5 μm) and (0.30–0.45 $\mu\text{m}^2/\text{ms}$), respectively (Palombo et al., 2016b).

Prior models used to clarify which aspects of tissue microstructure mostly affect metabolites DW-MRS signal have generally focused on relatively simple geometrical descriptions of the cellular microenvironment (spheres, randomly oriented cylinders, etc...) (Najac et al., 2014, 2016; Palombo et al., 2016a, 2016b; Ligneul et al., 2016; Assaf and Cohen, 1999, 2000; Pfeuffer et al., 2000; Cohen and Assaf, 2002; Bar-Shir and Cohen, 2008; Kroenke et al., 2004; Yablonskiy and Sukstanskii, 2010a), neglecting finer morphological details which may have an important role. Neurites may exhibit focal enlargements separated by constrictions (*beading* or *varicosities*) which may slow down the diffusion process (Budde and Frank, 2010); dendrites of some types of neuron, like Purkinje cells, contain branches with high density of *spines*, which may trap and hinder diffusing molecules (Santamaria et al., 2006); and astrocytic and macroglial processes present additional small radial ramifications, i.e. *leaflets*, which may retard the diffusion process along the main branch (Bushong et al., 2004; Sosunov et al., 2014).

The beaded morphology was observed in the central nervous system after ischemia as a consequence of osmotic imbalance (Budde and Frank, 2010). Beading-induced changes in cell-membrane morphology were shown (by water DW-MRI experiments and simulation) to be sufficient to significantly hinder water mobility and thereby decrease the water measured apparent diffusion coefficient (ADC) (Budde and Frank, 2010; Baron et al., 2015). On the contrary, there are no studies investigating the effects of spines and leaflets morphologies on intracellular diffusion metrics derived by NMR techniques such as DW-MRS. A combined approach, using local photolysis of caged compounds with fluorescence imaging, was used to visualize molecular diffusion within dendrites of cerebellar Purkinje cells (Santamaria et al., 2006). Diffusion of a volume marker, fluorescein dextran, along

spiny dendrites was remarkably slow in comparison to its diffusion in smooth dendrites (Santamaria et al., 2006), suggesting that these kinds of finer cell structures may have a non-negligible effect on the metabolites DW-MRS signal and the corresponding estimated diffusion metrics.

In this study, by performing Monte-Carlo (M-C) simulations of many particles diffusing in cylindrical compartments with secondary structures mimicking spines, leaflets and beading of neuronal and glial processes, we investigate to what extent the diffusion-weighted signal of intracellular molecules is sensitive and specific to spines/leaflets density and length, compared to a "control" deviation from smooth cylinder like beading of different amplitude. Three different "realistic" acquisition schemes are simulated: short-diffusion time oscillating gradients; intermediate-diffusion time/high b-value stimulated echo and long-diffusion time/low b-value stimulated echo experiments. Finally, comparison between numerical and experimental results obtained *in vivo* in mouse brain suggests that metabolite DW-MRS may be used to *in vivo* estimate spines/leaflets density and length.

Materials and methods

Synthetic tissue models

We focus our analysis on two specific finer morphological characteristics (or secondary structures) of cellular branches: spines and leaflets. Beads are also considered to provide a "control" deviation from smooth cylinders, thereby assessing specificity of the predicted effects of spines and leaflets. Synthetic substrates mimicking such structures were generated using cylinders as basic geometries. An infinitely long cylinder of radius $a_0=1.0 \mu\text{m}$ represents the branch of a neuronal and glial cell process. Here only one fiber is simulated and the density of fibers is irrelevant because the molecules in the simulation stay within the cylinder and other secondary features. Many smaller cylinders are then connected to it in random radial directions to represent spines or leaflets. Spines consist of two concentric cylinders representing neck and head compartments (Fig. 1A). The size of these compartments was randomly varied within the range of published values for the healthy brain (Santamaria et al., 2006): neck diameter in the range 0.1–0.3 μm ; neck length ranged from 0.4–2.1 μm and head length was between 0.4 and 0.7 μm . Spine head diameter ranged from 0.5–0.7 μm , with a minimum ratio of head-to-neck diameter of 1.5. Leaflets are made of two concentric cylinders with different radius (Fig. 1B): the cylinder at the base has diameter in the range 0.5–0.8 μm and the apical one has diameter in the range 0.2–0.4 μm . The total length of the leaflets was varied in the range 0.5–6.0 μm (Bushong et al., 2004; Sosunov et al., 2014). The location of spines and leaflets along the main branch is random, according to their density Φ ranging from 0.0 to $6.0 \mu\text{m}^{-1}$. Beading-like fiber consists of cylinders, concentric to the

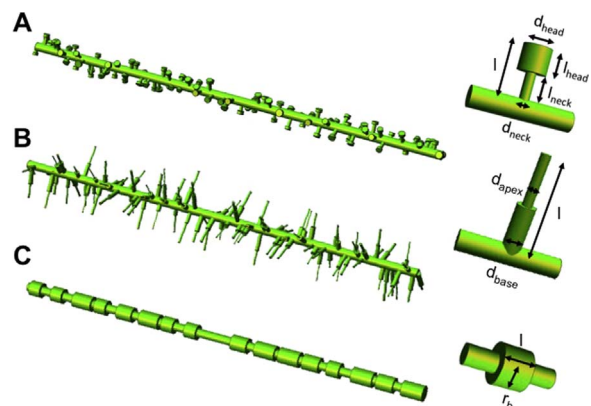


Fig. 1. Synthetic substrates mimicking three specific finer morphological characteristics (or secondary structures) of cellular branches: spines (A), leaflets (B) and beads (C).

main one representing the branch, with finite length in the range 0.2–1.0 μm and dimensionless beading amplitude: $A=(r_b-a_0)/(r_b+a_0)$, where r_b is the bead radius, ranging from 0.0 to 0.5 (Fig. 1C) (Budde and Frank, 2010). We investigated the effect of varying spine and leaflets density Φ and length l , and compared it with the effect of having non-smooth cylinder geometry by varying beading amplitude A on the metabolites diffusion process and corresponding DW-NMR signal. Specifically:

- varying spines/leaflets Φ in the range 0.0–6.0 μm^{-1} with length uniformly distributed in the physiological range 0.4–3.0 μm ;
- varying spines/leaflets l in the range 0.0–6.0 μm with density $\Phi=1 \mu\text{m}^{-1}$;
- varying beading amplitude A in the range 0.0–0.5 with beads separated by a distance uniformly distributed in the physiological range 2.0–4.0 μm .

Monte-Carlo data synthesis

The M-C modeling allows investigating the effect of mechanisms that are not included in analytical models. The approach maintains a population of “spins,” each executing a random walk within a tissue model of arbitrary complexity, described in details in the next section. In DW-NMR signal simulations, each spin has a magnetization that evolves depending on position and magnetic-field gradient at each time step.

A total of $N=10^5$ dimensionless spins were randomly placed in the synthetic substrate. A random walk at a rate $\Delta t=2.5 \times 10^{-2}$ ms per step, with bulk diffusivity (D_0) set to 0.5 $\mu\text{m}^2/\text{ms}$ and particle step size $\Delta r=(6D_0\Delta t)^{1/2}$ was performed according to the following rules:

1. perform the step Δx in a random direction in the three-dimensional space;
2. Check if the step crosses a barrier:
 1. if no barrier is crossed, the walker executes the step and updates its current position;
 2. if the step would take the walker across the barrier, the barrier elastically reflects the spin according to the simple rejection method (Johannesson and Halle, 1996). The step is rejected and the position of the spin remains unchanged.

From the set of particles trajectories obtained by M-C simulation, it is possible to compute some diffusion basic metrics which describe the dynamics of the diffusion process, independently of NMR measurement. One quantity investigated here is the diffusion coefficient, defined as:

$$D(t) = \frac{1}{2dt} \langle (\hat{n} \cdot \bar{r})^2 \rangle \quad (1)$$

where \bar{r} is the net displacement of a random walker during a diffusion time t in a given direction \hat{n} , in d dimensions. Considering \hat{n} parallel and orthogonal to the direction defining the axis of the main branch of the synthetic substrate simulated, the axial and radial diffusivities, $D_{\text{ax}}(t)$ and $D_{\text{rad}}(t)$, were computed.

Another diffusion metrics of interest is the dispersive diffusivity which can be obtained exactly from the Fourier Transform of the velocity autocorrelator (VCF):

$$D(\omega) = \int_{-\infty}^{\infty} dt \langle v(t)v(0) \rangle e^{i\omega t} \quad (2)$$

where ω is the angular frequency. We computed $VCF = \langle v(t)v(0) \rangle$ as $\partial_t^2 [tD(t)]$ and the corresponding $D(\omega)$ according to Eq. (2). Considering the direction \hat{n} being radial or axial, VCF_{rad} and VCF_{ax} were computed considering $D_{\text{rad}}(t)$ and $D_{\text{ax}}(t)$, respectively. $D_{\text{rad}}(\omega)$ and $D_{\text{ax}}(\omega)$ were then computed according to Eq. (2), while the isotropic dispersive

diffusivity $D(\omega)$ is computed as $[D_{\text{ax}}(\omega)+2D_{\text{rad}}(\omega)]/3$.

A phase accumulation approach is used to calculate the NMR signal. At each update in M-C loop (corresponding to time t), the j -th diffusing spin undergoes a phase variation $d\phi_j(t)$:

$$d\phi_j(t) = \gamma \vec{g}(t) \cdot \vec{x}_j(t) \Delta t \quad (3)$$

where $\vec{g}(t)$ is the gradient vector assumed constant over the time-step, and $\vec{x}_j(t)$ the j -th spin's position at time t . The synthetic signal is generated by summing the contributions from all the N spins at the end of the sequence (at time t_{seq}):

$$S_k = \left| \frac{1}{N} \sum_{j=1}^N e^{i\phi_j} \right| \quad (4)$$

where $\phi_j = \sum_{t=0}^{t_{\text{seq}}} d\phi_j(t)$.

Finally, it is straightforward to compute the ADC as:

$$ADC = - \frac{\ln(S/S_0)}{b} \quad (5)$$

where S_0 is the signal obtained without any diffusion sensitizing gradients (i.e. with $\vec{g}=0$) and b is the so called diffusion-weighting factor defined as:

$$b = \gamma^2 \int_0^{t_{\text{seq}}} dt \left[\int_0^t \vec{g}(t') dt' \right]^2 \quad (6)$$

Considering the signal obtained by applying the diffusion sensitizing gradients along the axial and radial direction, with respect to the axis of the main branch of the synthetic substrate simulated, the axial and radial ADC (ADC_{ax} and ADC_{rad}) were computed using Eq. (5), respectively.

Each numerical experiment was repeated 20 times, generating a new synthetic substrate (cylinder+secondary structures) each time, and the simulated DW-signals were averaged across the repeated experiments to minimize the deviation from the M-C simulation, as suggested in Hall and Alexander (2009). The relative SD of the simulated DW-signal was $< 1 \times 10^{-3}$. The simulations were implemented in MATLAB (The Mathworks) and performed using on a workstation equipped with two multi-core CPU Intel Xeon E5-2620 64 bit at 2.10 GHz, and a Nvidia GPU Tesla K20c with 2496 CUDA cores at 700 MHz. The random walk and the phase-accumulation computation kernels were run in parallel on GPU, while the signal computing kernel was run in parallel on CPUs. This highly parallelized approach allowed keeping the total computational time required for every single simulation ($N=10^5$ particles in a given geometry for a given sequence) lower than 1 h.

Simulations were used to investigate the effect of the presence of finer morphological details like spines, leaflets and beads on three different types of DW-NMR experiments, as described in deeper details in the next sections:

- ADC time-dependence at long diffusion times;
- High b values DW-NMR signal decay dependence;
- High frequency (short diffusion time) dispersive diffusivity dependence.

ADC time-dependence at long diffusion times

Brain metabolites ADC dependence at long diffusion time has recently been used to quantify and extract cell morphology and complexity (Palombo et al., 2016a). Whether and how spines and leaflets affect metabolites ADC time dependence at long t_d is still an open issue, which we want to deeper investigate in this work.

A pulsed-gradient stimulated echo (PGSTE) sequence with $\delta=3$ ms, $t_d=25, 60, 75, 100, 150, 200, 400, 800, 1000$ ms, $b=0$ and $6.5 \text{ ms}/\mu\text{m}^2$ and diffusion sensitizing gradient oriented along 1024 different directions chosen to be uniformly distributed on the unit sphere's surface was simulated to compute the total DW-NMR signal as the average of

the signal along each direction. For each t_d , the ADC, ADC_{ax} and ADC_{rad} were computed according to Eq. (5) using the average of the signal along each direction, the signal obtained by applying the diffusion sensitizing gradient along the axial direction and the signal obtained by using diffusion sensitizing gradient oriented along the radial direction, respectively.

High b values DW-NMR signal decay simulation

High b values DW-NMR experiments have already been used to extract cell branch diameter from metabolites DW-MRS data (Palombo et al., 2016b). Here we want to study if spines and leaflets may bias cell branch diameter estimation and in which way.

A PGSTE sequence with $\delta=3$ ms, $t_d=60$ ms, b ranging from 0 to 65 $ms/\mu m^2$ in steps of 3.25 $ms/\mu m^2$ was simulated for different values of spines and leaflets density $\Phi=0.0-6.0 \mu m^{-1}$ and length $l=0.0-6.0 \mu m$; and compared with different beading amplitudes $A=0.0-0.5$. The total DW-NMR signal coming from a large spectroscopic voxel in the brain is assumed to represent the sum of signals from a large number of differently oriented branches. Thus diffusion sensitizing gradients oriented along 1024 different directions chosen to be uniformly distributed on the unit sphere's surface were simulated and the total signal computed as their average.

In order to show the effects of the secondary structures investigated in this work in case of organised cylinders, like in white matter case, we have also investigated the signal decay as a function of b for the axial and radial direction to the fiber axis, individually.

High frequency (short diffusion time) dispersive diffusivity simulation

It is well known that short t_d measurements of the ADC of molecules diffusing in restricted systems can be used to extract geometric parameters of restricted pores, like the surface-to-volume ratio, S/V (Novikov and Kiselev, 2011; Schachter et al., 2000; Parsons et al., 2006; Xu et al., 2009). However, a promising way to get into the short-time limit is to apply the oscillating gradient (OG) method (Novikov and Kiselev, 2011; Schachter et al., 2000; Parsons et al., 2006; Xu et al., 2009), where the diffusion weighting is effectively accumulated over many periods of oscillation. In this way, it is in practice possible to measure very short diffusion times, i.e. less than milliseconds. In view of applying the OG techniques, the frequency dependence of the dispersive diffusivity, $D(\omega)$, rather than the t_d dependence of the ADC(t_d), is of great interest, as OG measurements can ideally directly measure $D(\omega)$. The $D_{rad}(\omega)$, $D_{ax}(\omega)$ and $D(\omega)$ frequency dependences were computed from simulated data as described in *Monte-Carlo data synthesis* section for different values of spines and leaflets density $\Phi=0.0-6.0 \mu m^{-1}$ and length $l=0.0-6.0 \mu m$; and compared with different beading amplitudes $A=0.0-0.5$ (as for the high b value simulations, described in the previous section).

Analysis of simulated data using analytical models

High b values PGSTE signal – randomly oriented hollow cylinders model

The synthetic signal simulated for high b values PGSTE experiments is analyzed with the analytical model recently used to quantify cell branch diameter (Palombo et al., 2016b), where cellular processes are described in first approximation as a collection of long cylinders without any secondary structure, with radius a and intracellular diffusivity D_{intra} . We assume cylinders randomly oriented to calculate signal attenuation in the narrow pulse approximation. The signal represents the sum of signals from within a large number of differently oriented fibers. For any given fiber, the axis makes a variable angle θ with the diffusion gradient, leading to two diffusion regimes: i) restricted diffusion in the plan perpendicular to their axis resulting in an effective gradient strength $g \sin(\theta)$ and ii) free diffusion in the

direction parallel to their axis resulting in an effective gradient strength $g \cos(\theta)$.

When the gradient is separated by an angle θ relative to the axis of the cylinder of radius a , the echo attenuation is given by the following expressions (Linse and Soderman, 1995):

$$E_{cyl}^a(g, \delta, t_d) = \left\{ \frac{[2J_1 \gamma g_{\perp} \delta a]^2}{(\gamma g_{\perp} \delta a)^2} + 8(\gamma g_{\parallel} \delta a)^2 B \right\} e^{-D_{intra}(\gamma g_{\parallel} \delta)^2 t_d} \quad (7)$$

with

$$B = \sum_{n=0}^{\infty} \left\{ \frac{1}{1 + \delta_{n0}} [J'_n \gamma g_{\perp} \delta a]^2 \sum_{m=1}^{\infty} \frac{\alpha_{nm}^2}{(\alpha_{nm}^2 - n^2)[\alpha_{nm}^2 - (\gamma g_{\perp} \delta a)^2]^2} e^{-\frac{D_{intra} \alpha_{nm}^2 t_d}{a^2}} \right\}$$

and $g_{\perp} = g \sin(\theta)$; $g_{\parallel} = g \cos(\theta)$.

In the above equations, J_n is the Bessel function of integer order n and α_{nm} is the m th positive root of the Bessel equation $J'_n=0$. δ_{n0} is the Kronecker delta symbol and D_{intra} is the free diffusivity, i.e. the diffusivity along the axis of the cylinder (often even called D_{\parallel}).

This theoretical attenuation (Eq. (7)) is used to fit synthetic signal decay as a function of b to estimate D_{intra}^{cyl} , a and the apparent S/V ratio for cylinders, i.e. $S/V_{app}=2/a$, for the different Φ , l and A values and investigate the dependence of model parameters on them. The error on estimated parameters was evaluated using a Monte Carlo approach ($N=2500$ draws). For each draw, random noise (whose standard deviation (SD) was estimated from the difference between the best fit and the data) was generated and added to the best fit to generate a new data set, which could be analyzed using the model.

Dispersive diffusivity at high frequencies – Mitra limit

The universal high frequency (i.e. short t_d) limit of the dispersive diffusivity is Novikov and Kiselev (2011):

$$D(\omega) = D_0 \left(1 - \frac{1}{\sqrt{2}d} S/V_{app} \sqrt{\frac{D_0}{\omega}} \right) \quad (8)$$

in d dimensions.

By fitting Eq. (8) to the high frequency behavior of $D(\omega)$ it is then possible to measure the apparent S/V ratio, S/V_{app} , of the specific geometry confining the molecules' diffusion without any assumption on its shape, and the molecules' bulk diffusivity, D_0 . These values are compared with those estimated by the hollow cylinder geometrical model described in the previous paragraph. The error on estimated parameters was evaluated using the Monte Carlo approach ($N=2500$ draws).

Results

Effect of spines, leaflets and beads on intracellular ADC diffusion time dependence

Preliminary simulations showed that using healthy physiological conditions for spines and leaflets geometry, the dynamics of particles diffusing inside them is not different within the error due to the relative SD of numerical simulations. In other words, we found that this configuration of spines and leaflets produces similar diffusion dynamics and DW-NMR signal for the two different structures. This is in agreement with results obtained by Santamaria et al. (2006) which investigated different spine's geometries by using numerical simulations. In fact, for spines geometries reflecting healthy physiological conditions, and for spines deformed in their shape in such a way to become close to leaflets shape (head diameter equal to neck diameter and total length 3 μm), Santamaria et al. (2006) observed almost the same dynamics (i.e. similar anomalous diffusion exponents and tortuosity values). For this reason, from now on, we will refer to spines/leaflets structure, without distinguish between spines and leaflets.

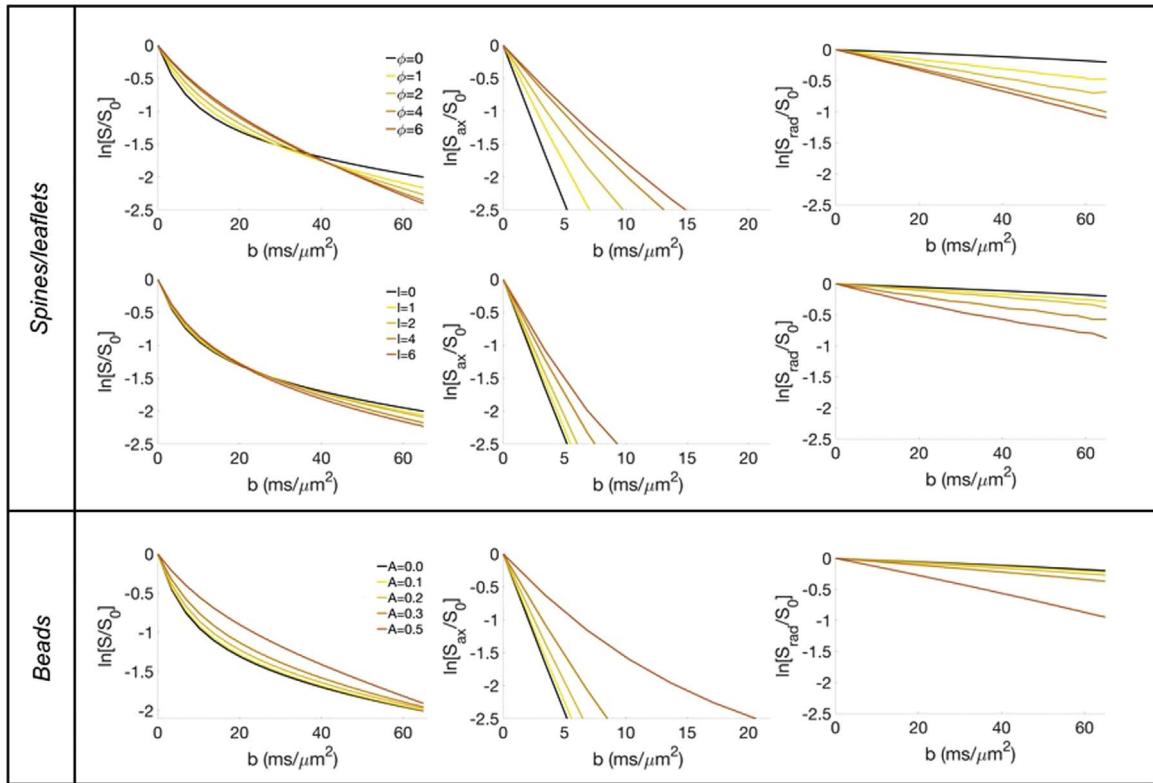


Fig. 2. Intracellular isotropic ADC (*left*) as a function of t_d for the different spines/leaflets densities (with $0.4 \leq l \leq 3.0 \mu\text{m}$), lengths (with $\Phi = 1.0 \mu\text{m}^{-1}$) and beading amplitudes as described in the inset legend. In order to fully appreciate the ADC time dependence, axial ADC_{ax} (*center*) and radial ADC_{rad} (*right*) values as a function of $1/t^{0.5}$ and $1/t$, respectively, are reported. Dashed black lines in ADC_{ax} plots (*center*) are the fits of the linear function $\text{ADC}_{\text{ax}}(t) = \text{ADC}(t = \infty) + C/t^{0.5}$, according to [Burcaw et al. \(2015\)](#). The R^2 of all the fits are larger than 0.95, showing the good agreement of the simulated data with the theoretical prediction ([Burcaw et al., 2015](#)). Simulated ADC_{ax} as a function of $1/t^{0.5}$ at very long t_d exhibit a plateau-like behavior due to intrinsic limit in numerical precision of the simulations.

Results of M-C molecular diffusion simulations in complex synthetic substrates mimicking neurites branches with spines, leaflets and beads are reported in [Fig. 2](#). Specifically, intracellular ADC values as a function of t_d are reported in [Fig. 2](#) (left column) for different values of spines/leaflets density $\Phi = 0.0\text{--}6.0 \mu\text{m}^{-1}$; spines/leaflets length $l = 0.0\text{--}6.0 \mu\text{m}$; and beading amplitude $A = 0.0\text{--}0.5$. The expected asymptotic behavior of the ADC at long t_d is observed, reaching the tortuosity behavior, i.e. not observable significant changes in ADC for $t_d > 200$ ms, for all spines/leaflets density or length (or beading amplitude). However, the asymptotic diffusivity at long t_d , $\text{ADC}(t_d = \infty)$, and thus the tortuosity τ , defined as $\text{ADC}(t_d = 0)/\text{ADC}(t_d = \infty)$, depends instead on Φ , l and A , as shown in [Fig. 2](#) (left column) and quantitatively reported in [Table 1](#).

In [Fig. 2](#) (central and right columns), the axial ADC, ADC_{ax} , time dependence as a function of $1/t^{0.5}$ and radial ADC, ADC_{rad} , as a function of $1/t$ are reported to fully appreciate their time dependence. We decided to plot ADC_{ax} as a function of $1/t^{0.5}$ to show the expected time dependence at long diffusion time for the molecular diffusivity in the presence of one-dimensional short range disorder, introduced in the axial direction by the randomly placed spines/leaflets (or beads), and ADC_{rad} as a function of $1/t$ to show the $\text{ADC} \rightarrow 0$ as $t \rightarrow \infty$ limiting behaviour for restricted diffusion in the direction radial to the fibers, according to [Burcaw et al. \(2015\)](#).

Effect of spines, leaflets and beads on high b values DW-NMR data and parameter estimates

Simulated normalized mean DW-MR signal attenuations as a function of b for different spines/leaflets densities, lengths and beading amplitudes are reported in [Fig. 3](#) (left column). It is possible to observe a clear dependence of the signal attenuation on Φ , l and A , which is different for each of the three morphological parameters investigated.

Qualitatively, signal attenuation is less pronounced as Φ , l and A increase, suggesting a reduction of the measured diffusivity. Moreover, a change in the curvature of the signal suggests an increase of the measured branch radius. In order to be more quantitative, these synthetic signal attenuations were fitted with [Eq. \(7\)](#) and the estimated a , D_{intra} and S/V_{app} values are reported in [Table 1](#), as a function of Φ , l and A . We found that branch radius is increasingly overestimated as Φ , l and A increase and D_{intra} is progressively underestimated as Φ , l and A increase. Values in [Table 1](#) show that, in the realistic experimental conditions simulated, model parameters (i.e. a and D_{intra}) dependence on Φ and l , in case of spines/leaflets presence, is not negligible for Φ and l within physiological ranges, leading to more than two-fold overestimation of a (corresponding to an underestimation of S/V_{app}) and underestimation of D_{intra} in case of very dense or very long secondary structures. Specifically, for substantial changes in Φ (from 0 to $6 \mu\text{m}^{-1}$), l (from 0 to $6 \mu\text{m}$) and A (from 0.0 to 0.5), a is overestimated up to $\sim 250\%$, $\sim 200\%$ and $\sim 250\%$, respectively; while D_{intra} is underestimated up to $\sim 60\%$, $\sim 20\%$ and $\sim 60\%$, respectively.

Finally, beading seems to have the most important effect in biasing model parameter estimation for $A > 0.2$ ([Table 1](#)). However, values of $A > 0.2$ are expected only in pathological conditions (ischemia), while in healthy conditions $A < 0.1$ is expected in the central nervous system ([Budde and Frank, 2010](#)). In fact, beads have been described as axonal, hence more likely localized to white matter, transient (as short as milliseconds) structures that arise as a consequence of neurophysiological distress. This suggests that in healthy conditions, beads should affect model parameter estimation in a negligible way.

In order to show the effects of the secondary structures investigated in this work in the case of organised cylinders, e.g. fiber bundles like in white matter, we reported DW-MR signal decay as a function of b for the axial and radial direction to the fiber axis, individually ([Fig. 3](#), central and left column). We observe that the axial DW-MR signal

Table 1

Model parameters (intracellular diffusivity, D_{intra} , cell fiber radius, a , apparent Surface-to-volume ratio, S/V_{app} , Intracellular space tortuosity, τ) and system properties (actual S/V ratio) estimated from the simulations of different morphologies. The percentage difference in diffusivity and S/V_{app} estimation, ΔD and $\Delta S/V_{\text{app}}$, between OG and PGSTE data is also reported. * apparent cell fiber radius estimated from the estimate of S/V_{app} , assuming a smooth hollow cylinder: $a=2/(S/V_{\text{app}})$.

Spines/Leaflets density ($0.4 \leq l \leq 3.0 \mu\text{m}$)			From PGSTE high b values (Randomly Oriented Cylinders model)			From OG high frequencies (Mitra regime)			Actual S/V (μm^{-1})	ΔD (%)	$\Delta S/V_{\text{app}}$ (%)	From long t_d
Φ (μm^{-1})	D_{intra} ($\mu\text{m}^2/\text{ms}$)	a (μm)	S/V_{app} (μm^{-1})	D_0 ($\mu\text{m}^2/\text{ms}$)	a^* (μm)	S/V_{app} (μm^{-1})					τ	
0	0.50 ± 0.01	1.02 ± 0.02	1.96 ± 0.05	0.50 ± 0.01	0.98 ± 0.02	2.05 ± 0.05	2.00	0.0	-4.4		1.00 ± 0.05	
1	0.37 ± 0.01	1.79 ± 0.10	1.11 ± 0.08	0.44 ± 0.01	0.91 ± 0.04	2.20 ± 0.05	2.20	-15	-50		1.35 ± 0.07	
2	0.29 ± 0.01	2.19 ± 0.10	0.91 ± 0.08	0.40 ± 0.01	0.86 ± 0.08	2.32 ± 0.08	2.32	-27	-61		1.52 ± 0.07	
4	0.21 ± 0.01	2.56 ± 0.12	0.78 ± 0.08	0.36 ± 0.01	0.81 ± 0.08	2.46 ± 0.08	2.48	-41	-68		1.98 ± 0.08	
6	0.19 ± 0.02	2.70 ± 0.12	0.74 ± 0.08	0.37 ± 0.01	0.78 ± 0.08	2.61 ± 0.08	2.60	-49	-72		2.17 ± 0.09	

Spines/Leaflets length ($\Phi=1.0 \mu\text{m}^{-1}$)			From PGSTE high b values (Randomly Oriented Cylinders model)			From OG high frequencies (Mitra regime)			Actual S/V (μm^{-1})	ΔD (%)	$\Delta S/V_{\text{app}}$ (%)	From long t_d
l (μm)	D_{intra} ($\mu\text{m}^2/\text{ms}$)	a (μm)	S/V_{app} (μm^{-1})	D_0 ($\mu\text{m}^2/\text{ms}$)	a^* (μm)	S/V_{app} (μm^{-1})					τ	
0	0.50 ± 0.01	1.06 ± 0.02	1.89 ± 0.05	0.50 ± 0.01	0.98 ± 0.02	2.05 ± 0.05	2.00	0.0	-7.8		1.00 ± 0.05	
1	0.46 ± 0.01	1.29 ± 0.10	1.55 ± 0.08	0.47 ± 0.01	1.02 ± 0.08	1.96 ± 0.08	2.04	-2.1	-21		1.05 ± 0.05	
2	0.43 ± 0.01	1.48 ± 0.10	1.35 ± 0.08	0.43 ± 0.01	0.99 ± 0.08	2.02 ± 0.08	2.08	0.0	-33		1.11 ± 0.05	
4	0.38 ± 0.01	1.83 ± 0.10	1.10 ± 0.08	0.40 ± 0.01	0.91 ± 0.08	2.19 ± 0.08	2.16	-5.0	-50		1.24 ± 0.06	
6	0.37 ± 0.02	1.96 ± 0.12	1.02 ± 0.08	0.37 ± 0.01	0.89 ± 0.08	2.25 ± 0.08	2.24	0.0	-55		1.28 ± 0.06	

Beads			From PGSTE high b values (Randomly Oriented Cylinders model)			From OG high frequencies (Mitra regime)			Actual S/V (μm^{-1})	ΔD (%)	$\Delta S/V_{\text{app}}$ (%)	From long t_d
A	D_{intra} ($\mu\text{m}^2/\text{ms}$)	a (μm)	S/V_{app} (μm^{-1})	D_0 ($\mu\text{m}^2/\text{ms}$)	a^* (μm)	S/V_{app} (μm^{-1})					τ	
0	0.50 ± 0.01	1.02 ± 0.02	1.96 ± 0.05	0.50 ± 0.01	0.98 ± 0.02	2.05 ± 0.05	2.00	0.0	-4.4		1.00 ± 0.05	
0.1	0.46 ± 0.01	1.11 ± 0.08	1.81 ± 0.08	0.49 ± 0.01	1.03 ± 0.04	1.94 ± 0.05	1.94	-6.1	-6.7		1.04 ± 0.05	
0.2	0.40 ± 0.01	1.25 ± 0.10	1.60 ± 0.08	0.48 ± 0.01	1.10 ± 0.04	1.81 ± 0.05	1.83	-17	-12		1.18 ± 0.06	
0.3	0.32 ± 0.01	1.50 ± 0.10	1.34 ± 0.08	0.47 ± 0.01	1.16 ± 0.04	1.73 ± 0.05	1.73	-32	-23		1.43 ± 0.07	
0.5	0.18 ± 0.01	2.34 ± 0.10	0.85 ± 0.08	0.44 ± 0.01	1.31 ± 0.05	1.53 ± 0.05	1.52	-59	-44		2.50 ± 0.09	

(Fig. 3, central column) exhibits increasingly non-monoexponential decay as a function of b as spines/leaflets Φ and l increase (or beads A increases), suggesting that diffusion along the axis of the fiber is non-Gaussian due to the presence of the secondary structures, in very good agreement with results and their interpretation reported by Yablonskiy and Sukstanskii (2010b). On the other hand, the radial DW-MR signal decay as a function of b (Fig. 3, right column) exhibits an attenuation compatible with diffusion in cylindrical geometry with radius increasing as spines/leaflets Φ and l increase (or beads A increases), when measured with diffusion sensitizing gradients orthogonal to cylinder axis (Eq. (7)).

Spines, leaflets and beads effects on high frequency DW-NMR data and parameter estimates

Isotropic, axial and radial dispersive diffusivities, $\text{ADC}(\omega)$, $\text{ADC}_{\text{ax}}(\omega)$ and $\text{ADC}_{\text{rad}}(\omega)$ as a function of ω are reported in Fig. 4. Like for the high b values results shown in the previous section, it is possible to observe a clear dependence of the dispersive diffusivities' behavior as a function of frequency on Φ , l and A , which is different for each of the three morphological parameters investigated. Qualitatively, we notice that $\text{ADC}_{\text{ax}}(\omega)$ is not constant as a function of ω at increasing values of Φ , l and A , consistent with an increase in the hindering of the axial diffusion process; $\text{ADC}_{\text{rad}}(\omega)$ increases the slope of how it approaches $\omega=0$ at increasing values of Φ , l and A , consistent with an increase in the size of the compartment restricting the diffusion in the radial plane. In order to be quantitative, we report the expected behavior of $\text{ADC}_{\text{rad}}(\omega)$ as a function of ω in the case of randomly oriented smooth cylinders, according to the analytical solution for diffusion in hollow cylinders reported in Linse and Soderman (1995), and shown in Fig. 5 as dashed lines. We found that the analytical

predictions for diffusion in smooth cylinders clearly fail in describing the $\text{ADC}_{\text{rad}}(\omega)$ behavior as a function of ω at increasing values of Φ and l , while it is still a good approximation in the presence of beads. On the contrary, $\text{ADC}(\omega)$ as a function of $\omega^{-1/2}$ is reported in Fig. 5, showing a good linear trend at high frequency (as expected within the Mitra regime). In this case, Eq. (8) was instead fitted to simulated isotropic dispersive diffusivity $\text{ADC}(\omega)$ to estimate S/V_{app} ratio and shown in Fig. 5 as dashed lines, for smooth cylinder and a representative condition in presence of spines, leaflets and beads. The extracted values of D_{intra} , a and S/V_{app} are reported in Table 1.

The actual S/V ratio for the simulated synthetic substrates can be exactly computed. For a perfect hollow cylinder of internal radius a_0 , we have $S/V=2/a_0$. The presence of spines, leaflets and beads will change the S/V ratio of cell's branch, according to the new morphology. Spines or leaflets can be approximated as radial secondary structure of cylindrical shape with radius r and length l , attached to the main branch of radius a_0 according to their density ϕ . In this approximation, the expected S/V for spines and leaflets is $\frac{S}{V} = \frac{2(a_0+r\phi)}{a_0^2+r^2\phi}$, which is larger than $2/a_0$ if $r < a_0$, that is the case of biological interest. On the contrary, beads can be approximated as cylinders of length l , radius r_b , and distributed along the branch of total length L in number N_b such that $N_b l \leq L$. In this approximation, the expected S/V for beads is $\frac{S}{V} = \frac{2[a_0 L + \frac{2A}{1-A} a_0 N_b l]}{a_0^2 L + \frac{4A}{(1-A)^2} a_0^2 N_b l}$, that is smaller than $2/a_0$ if $A < 1$, which is the case of biological interest. The actual S/V values for the different synthetic structures simulated are reported in Table 1, assuming for r the average value between head and neck. Results reported in Table 1 show that the apparent S/V ratio estimated by fitting Eq. (8) to numerical simulations results in the Mitra regime are actually in perfect agreement with the "true" values for the geometrical structures simulated, showing, for

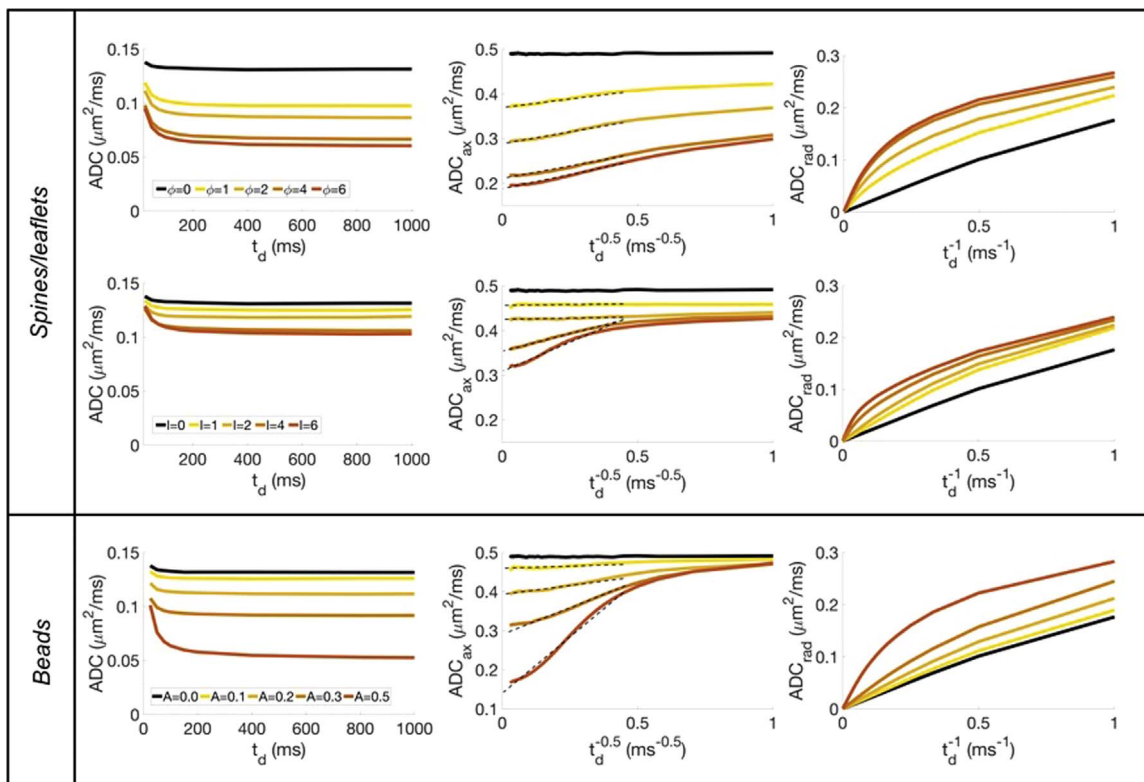


Fig. 3. Simulated normalized mean DW-MR signal attenuations as a function of b for different spines/leaflets densities (with $0.4 \leq l \leq 3.0 \mu\text{m}$), lengths (with $\Phi = 1.0 \mu\text{m}^{-1}$) and beading amplitudes as described in the inset legend (left). DW-MR signal decay as a function of b for the axial (centre) and radial (right) direction to the fiber axis are reported. The axial DW-MR signals (centre) exhibit increasingly non-monoexponential decay as a function of b as Φ and l increase (or beads A increases), suggesting that diffusion along the axis of the fiber is non-Gaussian due to the presence of the secondary structures. On the other hand, the radial DW-MR signal decays as a function of b (right) exhibit an attenuation compatible with diffusion in cylindrical geometry with radius increasing as Φ and l increase (or beads A increases).

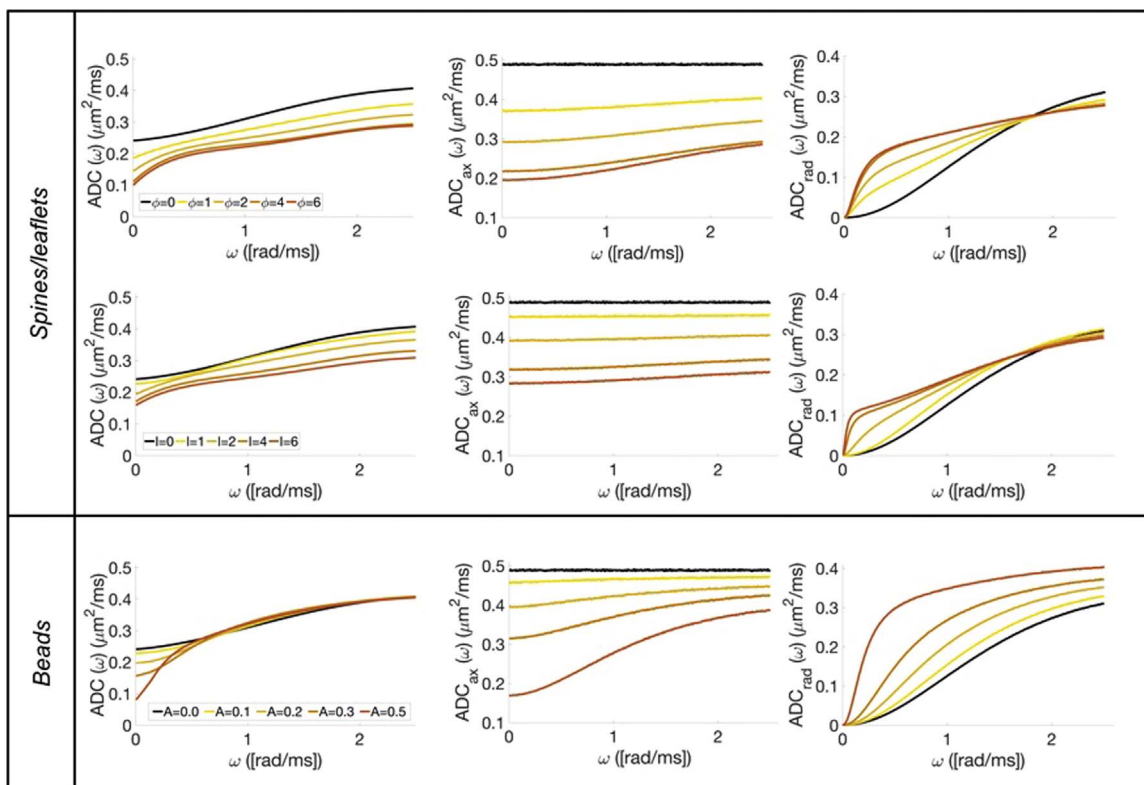


Fig. 4. Isotropic (left), axial (centre) and radial (right) dispersive diffusivities, ADC , ADC_{ax} and ADC_{rad} as a function of frequency, ω , for different spines/leaflets densities, lengths and beading amplitudes as described in the inset legend (left). A clear dependence of the dispersive diffusivities' behavior as a function of ω on Φ , l and A is shown.

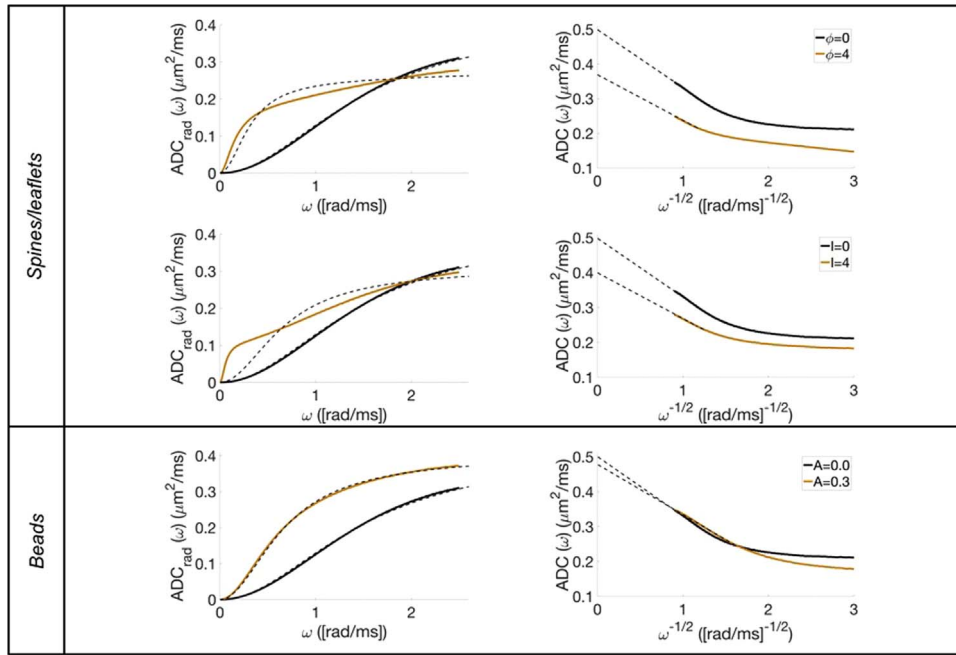


Fig. 5. $ADC_{rad}(\omega)$ as a function of ω and $ADC(\omega)$ as a function of $\omega^{-1/2}$, for the smooth cylinder case and a representative case of spines/leaflets density ($\phi=4$), spines/leaflets length ($l=4$) and beading amplitude ($A=0.3$). (left) Dashed lines represent the analytical solution for diffusion in hollow cylinders reported in Linse and Soderman (1995). The analytical predictions for diffusion in smooth cylinders clearly fail in describing the $ADC_{rad}(\omega)$ behavior as a function of ω at values of ϕ and l greater than 0, while it is still a good approximation in the presence of beads. (right) $ADC(\omega)$ as a function of $\omega^{-1/2}$ shows a good linear trend at high frequency (as expected within the Mitra regime). In fact, dashed lines represent Eq. (8) fitted to $ADC(\omega)$ to estimate S/V_{app} ratio and D_{intra} (values reported in Table 1).

spines and leaflets, increasing S/V as a function of ϕ and l and always $\geq 2 \mu\text{m}^{-1}$, which is the S/V value for the simulated branch without any spines or leaflets (i.e. smooth hollow cylinder of radius $a_0=1 \mu\text{m}$); while, for beads, decreasing S/V as a function of A and always $\leq 2 \mu\text{m}^{-1}$.

PGSTE high b values and OG high frequency results in vivo experiments on mouse brain

In Fig. 6 we report experimental data collected *in vivo* in the mouse brain at 11.7 T: normalized signal attenuations as a function of b (up to $b=60 \text{ ms}/\mu\text{m}^2$ at $t_d=63 \text{ ms}$, corresponding to $q \sim 1 \mu\text{m}^{-1}$), obtained in Palombo et al. (2016b) by PGSTE experiments, and ADC frequency dependence at high frequencies (up to $\sim 250 \text{ Hz}$) obtained in Ligneul

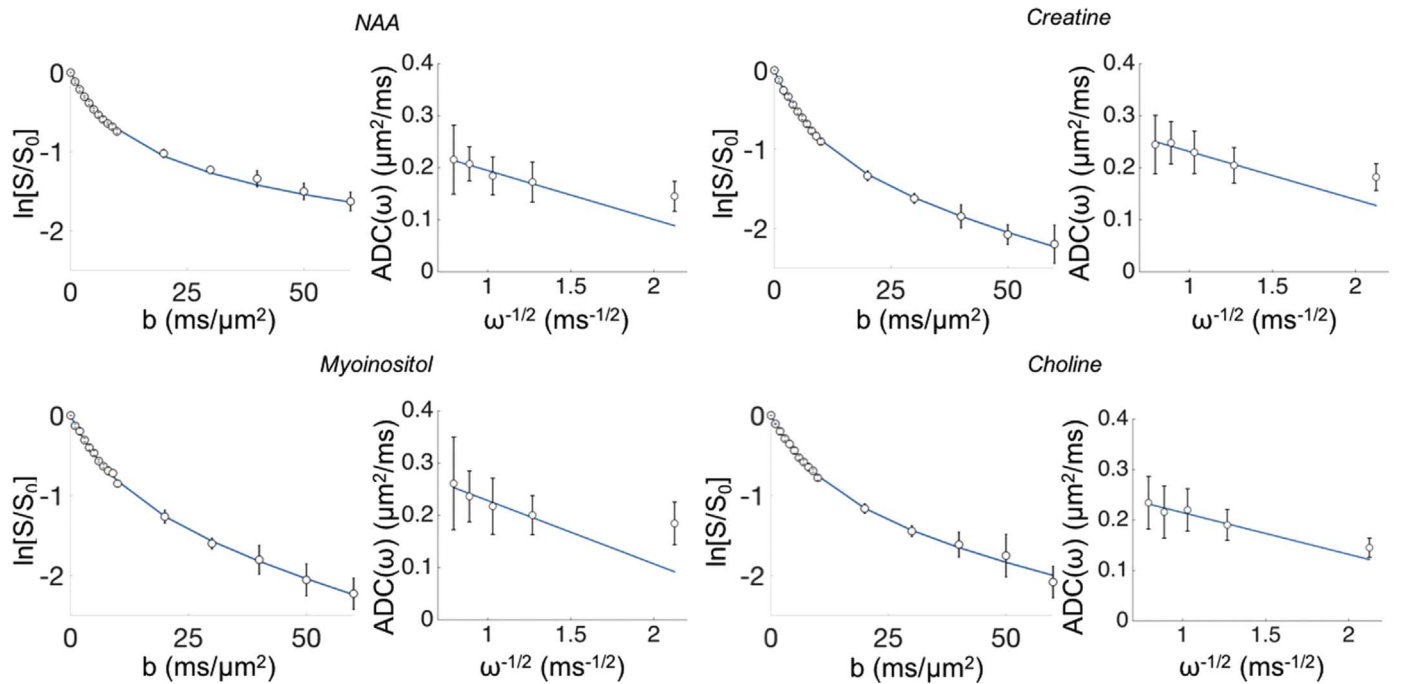


Fig. 6. Normalized signal attenuations as a function of b obtained in Palombo et al. (2016b) by PGSTE experiments, and ADC frequency dependence at high frequencies (up to $\sim 250 \text{ Hz}$) obtained in Ligneul and Valette (2016) by OG experiments, both *in vivo* in mouse brain, for some of the investigated brain metabolites. Straight lines represent fit of analytical expressions (Eqs. (7) and (8)) to experimental data. Error bars denote standard deviation.

Table 2

Model parameters (intracellular diffusivity, D_{intra} , cell fiber radius, a , apparent Surface-to-volume ratio, S/V_{app}) and the percentage difference in diffusivity and S/V_{app} estimation, ΔD and $\Delta S/V_{app}$, between OG and PGSTE data. * apparent cell fiber radius estimated from the estimate of S/V_{app} , assuming a smooth hollow cylinder: $a=2/(S/V_{app})$.

Metabolite	From PGSTE high b values (Randomly Oriented Cylinders model)			From OG high frequencies (Mitra regime)			ΔD (%)	$\Delta S/V_{app}$ (%)
	D_{intra} ($\mu\text{m}^2/\text{ms}$)	a (μm)	S/V_{app} (μm^{-1})	D_0 ($\mu\text{m}^2/\text{ms}$)	a^* (μm)	S/V_{app} (μm^{-1})		
NAA	0.33 ± 0.02	0.62 ± 0.12	3.23 ± 0.20	0.30 ± 0.01	0.78 ± 0.08	2.55 ± 0.05	10	26
Creatine	0.36 ± 0.02	1.43 ± 0.09	1.40 ± 0.08	0.32 ± 0.01	0.93 ± 0.08	2.16 ± 0.05	13	-45
Myoinositol	0.32 ± 0.02	1.55 ± 0.08	1.29 ± 0.10	0.35 ± 0.01	0.81 ± 0.08	2.46 ± 0.05	-8.6	-26
Choline	0.31 ± 0.02	1.26 ± 0.08	1.59 ± 0.10	0.30 ± 0.01	0.93 ± 0.08	2.14 ± 0.05	3.3	-44

and Valette (2016) by OG experiments, for some brain metabolites (NAA, Creatine, Choline and Myo-inositol). For details on experimental methods used to acquire the data, we refer the reader to Palombo et al. (2016b) and Ligneul and Valette (2016). Parameters extracted from the fits of PGSTE and OG experiments are reported in Table 2.

Discussion

Effect of secondary structures on measured intracellular diffusion

Despite the possibility to make high resolution images of the brain, water based DW-NMR techniques are expected to be less specific and sensitive to intracellular space changes than metabolite DW-MRS methods. This is due to the fact that: 1) metabolites are purely intracellular diffusing molecules, while water is ubiquitous in biological tissues; 2) metabolites are cell-specific probes, i.e. some of them mostly diffuse in specific different cell compartments: NAA and Glu within neurons, while tCho and Ins within macroglia (mostly astrocytes). We have recently proposed to use different DW-MRS techniques to quantitatively extract parameters directly related to cell morphology: number of consecutive embranchments and branch lengths (Palombo et al., 2016a) of neuronal and astrocytic neuritic trees, as well as branch diameter and intracellular diffusivity (Palombo et al., 2016b). However, these methods allow for the extraction of the cell's morphological features by making some assumptions on the geometry of the cellular compartments, i.e. by modeling cells as a combination of simple geometries (branched sticks and cylinders). High magnification histology images clearly show that this is a quite simplistic assumption, because brain cells, like neurons and astrocytes, have very complex topologies. In fact, while the "backbone" of the cell can be modeled using these simple geometries, secondary finer details like spines and leaflets (generally also called branchlets) are important structures which may bias parameter estimation in these simple models. Here we used M-C simulations to go one step further by investigating whether and how these finer morphological details have an effect on the measured metabolites diffusion by DW-MRS techniques. To summarize, the simulations show that:

- Estimated intracellular tortuosity increases as spines and leaflets density or length increase, and it increases as beading amplitude increases, but this last is negligible in healthy conditions ($A < 0.1$). These results also show that the effects of finer morphological details like spines and leaflets (and beads) is actually under the practical sensitivity of realistic experimental conditions at long t_d (i.e. $t_d > 200$ ms), suggesting that modeling of long- t_d data based on solely long-range morphological features should be preferentially done at $t_d > 200$ ms. Numerical simulation results reported in this work refer to metabolites diffusion. Because water molecules diffuse about three times faster than metabolites, these results can be opportunely scaled to be extended to water diffusion in the intracellular space. For example, results reported here show that the tortuosity limit is

always reached for $t_d > 200$ ms (and even before for low $\Phi/l/A$). This suggests that, for intracellular water, tortuosity limit is reached for $t_d > 70$ ms (i.e. the effects of secondary structures are expected to affect the ADC time dependence for $t_d > 70$ ms in a negligible way).

- Although a simple geometrical model based on modeling cell's branches like randomly oriented cylinders (Eq. (7)) accurately describes the high b values signal decay, the estimated model parameters values are biased by the presence of cellular finer morphological structures (Table 1). In the presence of secondary structures, branch diameter is overestimated, while intracellular diffusivity is underestimated (although the bias due to the presence of beads is negligible in healthy conditions, i.e. $A < 0.1$). This is quite intuitive: radial secondary structures hinder the longitudinal diffusion along the main branch, while they offer larger space for displacement along radial direction, effectively mimicking diffusion in a wider cylinder. As shown here by numerical simulations, this intuitive effect of secondary structures may significantly affect real DW-MRS experiments, at least those performed with sequence parameters similar to those simulated here. This suggests that DW-NMR signal from the intracellular compartment at high b values is quite sensitive to fine cell branch morphology. New analytical and/or numerical models, which include finer structures like spines and leaflets (and beads), are needed to properly describe the DW-NMR signal from intracellular space and they may be useful to measure spines and leaflets density and morphological properties (e.g. length or volume).
- Apparent S/V ratio estimated by linear fit of high frequency OG data appears to be an excellent estimation of the actual S/V ratio, even in the presence of secondary structures. This ratio increases as spines and leaflets density or length increase, while it decreases as beading amplitude increases, but the latter is negligible in physiological conditions ($A < 0.1$); In contrast, intracellular diffusivity as estimated by linear fit of high frequency OG data is underestimated, suggesting that diffusion may not strictly be in the Mitra regime yet, although S/V is already well estimated.

It is worth mentioning that axonal meandering or undulation, as well as cell fibers branching and finite length would have an impact on the tortuosity at long t_d , as well as on the ADC long time dependence and maybe the high b values DW-MR signal attenuation behaviour. However, in this work we did not investigate that, as it had already been done before (Palombo et al., 2016a; Nilsson et al., 2012; Ronen et al., 2014). Concerning the possible effect of axonal dispersion within the large spectroscopic voxel, in our recently published paper (Palombo et al., 2016b) we showed that the assumption of fibers isotropically distributed is a good approximation for the macroscopic DW-MR signal measured from the spectroscopic voxel.

Discrepancy between PGSTE high b and OG high frequency results

Interestingly, our numerical simulations of PGSTE high b and OG

high frequencies experiments show some discrepancy between the estimated parameters (intracellular diffusivity and apparent S/V ratio or corresponding branch radius) using the two DW-MRS techniques when secondary structures are present (Table 1). It is interesting to compare the apparent S/V ratio values obtained by OG experiments in the Mitra regime (i.e. the best estimation of the actual S/V ratio), with those obtained from PGSTE high b values datasets. It can be seen in Table 1 that, when secondary structures are present, PGSTE and OG data do not yield the same values for diffusivities and, most strikingly, for S/V_{app} . This difference can be quantified by computing the percentage difference in diffusivity and S/V_{app} estimation, ΔD and $\Delta S/V_{app}$, between OG and PGSTE data. From Table 1 here are the conclusions which can be drawn about the comparison between PGSTE and OG results:

- **Effect of φ on the discrepancy between parameters.** As expected, for $\varphi=0.0 \mu\text{m}^{-1}$, the two techniques provide the same estimation of diffusivity and S/V_{app} , within the 5% of uncertainty (i.e. $|\Delta D|$ and $|\Delta S/V_{app}|$ lower than 5%). As φ increases, the intracellular diffusivity and S/V_{app} are increasingly underestimated for PGSTE as compared to OG. In fact, ΔD and $\Delta S/V_{app}$ can reach -50% and -70% , respectively, when $\varphi=6.0 \mu\text{m}^{-1}$. S/V_{app} actually appears to be more biased than D, suggesting the necessity of defining novel analytical and/or numerical models for high-b PGSTE modeling including finer structures like spines, leaflets and beads, in order to better determine cell fibers diameter and intracellular diffusivity.
- **Effect of l on the discrepancy between parameters.** For $\varphi=0.0 \mu\text{m}^{-1}$, the two techniques provide the same estimation of diffusivity and S/V_{app} , within the 10% of uncertainty (i.e. $|\Delta D|$ and $|\Delta S/V_{app}|$ lower than 10%). Similarly to the effect of φ , S/V_{app} is increasingly underestimated for PGSTE as l increases, compared to OG ($\Delta S/V_{app}$ can reach -50% when $l=6.0 \mu\text{m}$). In contrast to φ , the discrepancy in intracellular diffusivity is much lower than in the case of increasing φ ($|\Delta D|$ always lower than 5%), although both techniques yield underestimated values compared to ground truth.
- **Effect of A on the discrepancy between parameters.** For $A=0.0$, the two techniques provide the same estimation of diffusivity and S/V_{app} , within the 5% of uncertainty (i.e. $|\Delta D|$ and $|\Delta S/V_{app}|$ lower than 5%). The intracellular diffusivity and S/V_{app} are both increasingly underestimated for PGSTE as A increases. ΔD and $\Delta S/V_{app}$ can reach -60% and -44% , respectively, when $A=0.5$. In contrast to spines/leaflets, in the case of beading, the intracellular diffusivity seems to be more biased than S/V_{app} when high b value PGSTE experiments are used instead of OG.

To summarize, in our simulations, high spines/leaflets density results in $\Delta S/V_{app} \ll \Delta D \ll 0$, long spines/leaflets results in $\Delta S/V_{app} \ll \Delta D \sim 0$, and strong beading results in $\Delta D \ll \Delta S/V_{app} \ll 0$. This discrepancy provides a potential way to look for the signature of secondary structures *in vivo*, where experimental data collected at high b and at high frequencies (Palombo et al., 2016b; Ligneul and Valette, 2016) can be confronted, as done in the next section.

Interpreting discrepancies between PGSTE high b values and OG high frequency results in in vivo experiments using numerical simulation results

High b values PGSTE data *in vivo* in mouse brain were obtained by using the same sequence parameters as simulated in this study, and modeled by using the simple geometrical model in Eq. (7) to estimate cell's branch radius, the corresponding S/V_{app} and intracellular diffusivity (Palombo et al., 2016b). These estimated values, for some relevant metabolites (NAA, tCr, Ins and tCho) are reported in Table 2. We compare these results with those we have recently obtained by performing OG ultra-short diffusion time ADC measurements *in*

in vivo in the same mouse brain and analyzed by using the Mitra regime asymptotic behavior (i.e. Eq. (8)). These data are published in Ligneul and Valette (2016) and here reported in Fig. 6 and Table 2. The two approaches provide quite different values for the estimated parameters (intracellular diffusivity and S/V_{app}). While for all the considered metabolites, except NAA, the estimated S/V_{app} values with PGSTE technique are considerably smaller (up to -45%) than those estimated by OG, the diffusivity values are the same within the 10% of uncertainty ($|\Delta D| \leq \pm 10\%$). When compared to values obtained by fitting simulated data (Table 1) these ΔD and $\Delta S/V_{app}$ values are coherent with a relatively low density of spines or leaflets ($\varphi \leq 1.0 \mu\text{m}^{-1}$) of moderate length ($l \leq 4.0 \mu\text{m}$), which is reasonable according to histology (Assaf and Cohen, 1999; Bushong et al., 2004; Sosunov et al., 2014). The fact that *in vivo* data do not yield largely negative ΔD precludes the existence of significant beading-like structures ($A \leq 0.1$), as expected in healthy conditions for the spectroscopic voxel considered. We should mention that for NAA we find a slightly positive $\Delta S/V_{app}$, which cannot be explained by secondary structures investigated here. However, as previously discussed in Palombo et al. (2016b), NAA represents a particular case. Indeed, a small fraction of NAA is supposed to be highly restricted in very small regions (like mitochondria or myelin sheaths). Finally, to be honest, the uncertainty on S/V_{app} estimated from high b for NAA is large, so this positive $\Delta S/V_{app}$ might be artefactual.

It is interesting to look what intracellular tortuosity to expect, based on the spines/leaflets density and length consistent with *in vivo* data. Looking at Table 1, it appears that intracellular tortuosity should be relatively low, i.e. less than ~ 1.3 , for $\varphi \leq 1.0 \mu\text{m}^{-1}$ and $l \leq 4.0 \mu\text{m}$.

Effect of experimental noise and SNR

In order to invoke practical conclusions from the numerical simulations results reported here, the effect of different SNR values on the estimated microstructural features was also considered. Gaussian noise was added to the simulated diffusion weighted signal decays at high b-values and different diffusion times in order to simulate three scenarios: SNR= ∞ (noise free case); 50 (good experimental conditions) and 10 (worse experimental conditions). We found that parameter estimation was not significantly biased by noise when SNR decreased from infinity to 10, suggesting that the effects of secondary structures discussed so far are of practical significance even in realistic experimental conditions.

Limitations

The main goal of this numerical study is to investigate if and how the presence of finer morphological structures (i.e. spines, leaflets and beads) on cell fibers can affect intracellular diffusion of brain metabolites and DW-MRS derived metrics. Although numerical simulation results presented here can be helpful to interpret experimental data, this study has some limitations. In particular, T_2 and T_1 relaxation effects were neglected. The potential correlation between brain metabolites diffusion and relaxation is of importance for interpreting and modeling metabolite diffusion based on pure geometry, irrespective of relaxation properties (multi-compartmental relaxation or surface relaxivity). For high b values and high frequencies simulations, relaxation effects can presumably be ignored, as we have recently shown that the correlation between relaxation and diffusion properties is extremely small or even nonexistent for metabolites in the mouse brain in this range of TE/TM, even though this might not be true in myelinated fibers (Ligneul et al., 2016). In long t_d experiments, the potential effect of T_1 relaxation during t_d is still an open issue. Specifically, potential wall relaxivity might exist and cause correlation between T_1 relaxation and diffusion properties, which was not considered here and is generally neglected in DW-NMR modeling, but could be added in the simulations. Although being of interest, this is far from the aim of this

study.

Conclusion

Here we used M-C numerical simulations to investigate to what extent secondary structures like spines, leaflets and beads have an effect on the measured metabolites diffusion by DW-MRS techniques. Results suggest that, in healthy physiological conditions, spines and leaflets density and length (Φ and l) bias cell branch diameter (overestimated) and intracellular diffusivity (underestimated) estimation. Compared with a “control” case of deviation from smooth cylinder assumption like in beading-like structure, we found that the effects of beads on cell branch diameter and intracellular diffusivity estimation is negligible, when fit is performed on high-b data with a simple model of cylinders. Moreover, we showed that intracellular tortuosity as determined at long t_d increases as spines and leaflets density or length increases; and it increases as beading amplitude (A) increases, but this increase is negligible in healthy physiological conditions ($A < 0.1$). The last result of this work is that S/V ratio estimated from linear fit of high-frequency data increases as spines and leaflets density or length increase, while S/V ratio decreases as beading amplitude increases, but this decrease is negligible in healthy physiological conditions ($A < 0.1$). Very interestingly, the bias on estimated parameters is different depending on the modality used (high-b or high-frequency acquisitions). This opens perspectives to assess and quantify the presence of secondary structures *in vivo*, by confronting experimental data acquired with these modalities. Despite some limitations, the results presented in this work are useful to help for the interpretations of experimental data, and they may be of interest for the DW-NMR community by stimulating future developments and applications, including secondary structure characterization in neurodegenerative diseases.

Acknowledgments

This work was supported by the European Research Council (“INCELL” project, ERC grant 336331). The 11.7 T MRI scanner was funded by a grant from “Investissements d’Avenir - ANR-11-INBS-0011” - NeurATRIS: A Translational Research Infrastructure for Biotherapies in Neurosciences.

References

Assaf, Y., Cohen, Y., 1999. Structural information in neuronal tissue as revealed by q-space diffusion NMR spectroscopy of metabolites in bovine optic nerve. *NMR Biomed.* 12 (6), 335–344.

Assaf, Y., Cohen, Y., 2000. Assignment of the water slow-diffusing component in the central nervous system using q-space diffusion MRS: implications for fiber tract imaging. *Magn. Reson. Med.* 43 (2), 191–199.

Baron, C.A., Kate, M., Gioia, L., Butcher, K., Emery, D., Budde, M., Beaulieu, C., 2015. Reduction of diffusion-weighted imaging contrast of acute ischemic stroke at short diffusion times. *Stroke* 46 (8), 2136–2141.

Bar-Shir, A., Cohen, Y., 2008. High b-value q-space diffusion MRS of nerves: structural information and comparison with histological evidence. *NMR Biomed.* 21 (2), 165–174.

Basser, P.J., Pierpaoli, C., 2011. Microstructural and physiological features of tissues elucidated by quantitative-diffusion-tensor MRI. 1996. *J Magn. Reson* 213 (2), 560–570.

Basser, P.J., Mattiello, J., LeBihan, D., 1994. MR diffusion tensor spectroscopy and imaging. *Biophys. J* 66 (1), 259–267.

Beaulieu, C., 2002. The basis of anisotropic water diffusion in the nervous system: a technical review. *NMR Biomed.* 15 (7–8), 435–455.

Budde, M.D., Frank, J.A., 2010. Neurite beading is sufficient to decrease the apparent diffusion coefficient after ischemic stroke. *Proc. Natl. Acad. Sci. USA.*

Burcaw, L.M., Fieremans, E., Novikov, D.S., 2015. Mesoscopic structure of neuronal tracts from time-dependent diffusion. *NeuroImage* 114, 18–37.

Bushong, E.A., Martone, M.E., Ellisman, M.H., 2004. Maturation of astrocyte

morphology and the establishment of astrocyte domains during postnatal hippocampal development. *Int. J. Dev. Neurosci.* 22 (2), 73–86.

Choi, J.K., Dedeoglu, A., Jenkins, B.G., 2007. Application of MRS to mouse models of neurodegenerative illness. *NMR Biomed.* 20 (3), 216–237.

Cohen, Y., Assaf, Y., 2002. High b-value q-space analyzed diffusion-weighted MRS and MRI in neuronal tissues—a technical review. *NMR Biomed.* 15 (7–8), 516–542.

Hall, M.G., Alexander, D.C., 2009. Convergence and parameter choice for Monte-Carlo simulations of diffusion MRI. *IEEE Trans. Med. Imaging* 28 (9), 1354–1364.

Johannesson, H., Halle, B., 1996. Solvent diffusion in ordered macrofluids: a stochastic simulation study of the obstruction effect. *J. Chem. Phys.* 104, 6807–6817.

Kroenke, C.D., Ackerman, J.J., Yablonskiy, D.A., 2004. On the nature of the NAA diffusion attenuated MR signal in the central nervous system. *Magn. Reson. Med.* 52 (5), 1052–1059.

Ligneul, C., Valette, J., 2016. Probing metabolite diffusion at ultra-short time scales in the mouse brain using optimized oscillating gradients and “short” echo time diffusion-weighted MR spectroscopy. *NMR Biomed.* <http://dx.doi.org/10.1002/nbm.3671>.

Ligneul, C., Palombo, M., Valette, J., 2016. Metabolite diffusion up to very high b in the mouse brain *in vivo*: revisiting the potential correlation between relaxation and diffusion properties. *Mag. Reson. Med.* <http://dx.doi.org/10.1002/mrm.26217>.

Linse, P., Soderman, O., 1995. The validity of the short-gradient-pulse approximation in NMR studies of restricted diffusion simulations of molecules diffusing between planes, in cylinders and spheres. *J. Magn. Reson. Ser. A* 116 (1), 77–86.

Najac, C., Marchadour, C., Guillermier, M., Houitte, D., Slavov, V., Brouillet, E., Hantraye, P., Lebon, V., Valette, J., 2014. Intracellular metabolites in the primate brain are primarily localized in long fibers rather than in cell bodies, as shown by diffusion-weighted magnetic resonance spectroscopy. *NeuroImage* 90, 374–380.

Najac, C., Branzoli, F., Ronen, I., Valette, J., 2016. Brain intracellular metabolites are freely diffusing along cell fibers in grey and white matter, as measured by diffusion-weighted MR spectroscopy in the human brain at 7 T. *Brain Struct. Funct.* 221 (3), 1245–1254.

Nicolay, K., Braun, K.P., Graaf, R.A., Di jkhuizen, R.M., Kruijskamp, M.J., 2001. Diffusion NMR spectroscopy. *NMR Biomed.* 14 (2), 94–111.

Nilsson, M., Lätt, J., Ståhlberg, F., Westén, D., Hagglätt, H., 2012. The importance of axonal undulation in diffusion MR measurements: a Monte Carlo simulation study. *NMR Biomed.* 25 (5), 795–805.

Norris, D.G., 2001. The effects of microscopic tissue parameters on the diffusion weighted magnetic resonance imaging experiment. *NMR Biomed.* 14 (2), 77–93.

Novikov, D.S., Kiselev, V.G., 2011. Surface-to-volume ratio with oscillating gradients. *J. Magn. Reson.* 210 (1), 141–145.

Palombo, M., Ligneul, C., Najac, C., Le Douce, J., Flament, J., Escartin, C., Hantraye, P., Brouillet, E., Bonvento, G., Valette, J., 2016a. New paradigm to assess brain cell morphology by diffusion-weighted MR spectroscopy *in vivo*. *Proc. Natl. Acad. Sci. USA* 113 (24), 6671–6676.

Palombo, M., Ligneul, C., Valette, J., 2016b. Modeling diffusion of intracellular metabolites in the mouse brain up to very high diffusion-weighting: diffusion in long fibers (almost) accounts for non-monoexponential attenuation. *Magn. Reson. Med.* <http://dx.doi.org/10.1002/mrm.26548>.

Parsons, E.C., Does, M.D., Gore, J.C., 2006. Temporal diffusion spectroscopy: theory and implementation in restricted systems using oscillating gradients. *Magn. Reson. Med.* 55 (1), 75–84.

Pfeuffer, J., Tkáč, I., Gruetter, R., 2000. Extracellular–intracellular distribution of glucose and lactate in the rat brain assessed noninvasively by diffusion-weighted 1H nuclear magnetic resonance spectroscopy *in vivo*. *J. Cereb. Blood Flow. Metab.* 20 (4), 736–746.

Ronen, I., Valette, J., 2015. Diffusion-weighted magnetic resonance spectroscopy. *eMagRes* 4, 733–750.

Ronen, I., Budde, M., Ercan, E., Annese, J., Techawiboonwong, A., Webb, A., 2014. Microstructural organization of axons in the human corpus callosum quantified by diffusion-weighted magnetic resonance spectroscopy of N-acetylaspartate and post-mortem histology. *Brain Struct Funct.* 219 (5), 1773–1785.

Santamaria, F., Wils, S., De Schutter, E., Augustine, G.J., 2006. Anomalous diffusion in Purkinje cell dendrites caused by spines. *Neuron* 52 (4), 635–648, (USA 107(32) 14472–14477).

Schachter, M., Does, M.D., Anderson, A.W., Gore, J.C., 2000. Measurements of restricted diffusion using an oscillating gradient spin-echo sequence. *J. Magn. Reson.* 147 (2), 232–237.

Sosunov, A.A., Wu, X., Tsankova, N.M., Guilfoyle, E., McKhann, G.M., Goldman, J.E., 2014. Phenotypic heterogeneity and plasticity of isocortical and hippocampal astrocytes in the human brain. *J. Neurosci.* 34 (6), 2285–2298.

Wedeen, V.J., et al., 2012. The geometric structure of the brain fiber pathways. *Science* 335 (6076), 1628–1634.

Xu, J., Does, M.D., Gore, J.C., 2009. Quantitative characterization of tissue microstructure with temporal diffusion spectroscopy. *J. Magn. Reson.* 200 (2), 189–197.

Yablonskiy, D.A., Sukstanskii, A.L., 2010a. Theoretical models of the diffusion weighted MR signal. *NMR Biomed.* 23 (7), 661–681.

Yablonskiy, D.A., Sukstanskii, A.L., 2010b. Theoretical models of the diffusion weighted MR signal. *NMR Biomed.* 23 (7), 661–681.